International Journal of Mechanical Sciences 150 (2019) 103–111

Contents lists available at ScienceDirect

International Journal of Mechanical Sciences

journal homepage: www.elsevier.com/locate/ijmecsci

Localised prior strain-hardening increases the tearing resistance of ductile steel

H.E. Coules[a,*], G.C.M. Horne[a], M.J. Peel[a], T. Connolley[b]

[a] Department of Mechanical Engineering, University of Bristol, Bristol, UK
[b] Diamond Light Source, Oxfordshire, UK

ARTICLE INFO

Keywords:
Ductile tearing
Digital image correlation
Energy-dispersive X-ray diffraction
Finite element analysis

ABSTRACT

In structural materials, 'intrinsic' toughening originates from plastic dissipation of strain energy at the tips of cracks. This depends on a material's microstructure and its stress–strain response. By introducing a spatially-varying distribution of prior strain-hardening into a material, we can modify the stress field which develops around a crack as it is loaded, producing an increased resistance to ductile tearing. We demonstrate this toughening effect using synchrotron X-ray diffraction and digital image correlation measurements of the crack tip region in a ductile ferritic steel. Localised strain-hardening also introduces a residual stress, but this is shown not to contribute significantly to the initiation of tearing in this material.

1. Introduction

Residual stresses occur in materials as the result of internal strain incompatibility. Despite being self-equilibrating, residual stresses can strongly influence a material's resistance to fracture [1]. Residual stress contributes to the rate at which strain energy is released during the advance of a crack, modifying the material's apparent toughness. In very brittle materials, residual stresses superimpose almost perfectly on any stress field caused by other forms of loading. In more ductile materials, plasticity may occur as residual and applied stresses superimpose causing partial stress relaxation. Therefore, the influence of residual stresses on fracture is typically strong under brittle conditions but weaker under ductile conditions [1–3].

The crack tip strain energy release rate in an ideal non-linear elastic material (i.e., a material in which the strain energy density is a single-valued function of the stress tensor) can be defined using the following contour integral [4,5]:

$$J = \int_{\Gamma} \left(W\delta_{1j} - \sigma_{ij}u_{i,1}\right)n_j\,ds \tag{1}$$

where W is the strain energy density, σ_{ij} is the stress tensor, u_i is the displacement vector and δ_{ij} is the Kronecker delta. s represents distance along a crack-tip-enclosing contour Γ, for which n_j is an outward-facing normal vector. In a non-linear elastic material, the J-integral also characterises the strength of the $\frac{1}{r}$ stress singularity at the crack tip [6,7]. While acknowledging that the crack tip stress field in real elastic–plastic materials deviates from the non-linear elastic case, a critical value of J can be used as an approximate criterion for fracture initiation [8,9]. In very ductile materials, where there is a significant discrepancy between the material's real behaviour and the deformation theory of plasticity, the J-integral is less representative. Several authors have attempted to address the non-proportionality of real materials by re-formulating the J-integral to take this effect into account [10,11].

Eq. (1) can become strongly contour-dependent in the presence of residual stresses, thermal stresses or tractions applied to the crack flank. To resolve the deficiencies of the J-integral when applied to structures that contain residual stress, Lei re-formulated it in a modified form based on an earlier analysis for thermal stress by Wilson and Yu [12–14]:

$$J_{mod} = \int_{\Gamma} \left(W\delta_{1j} - \sigma_{ij}u_{i,1}\right)n_j\,ds + \int_{A} \sigma_{ij}\varepsilon^{0}_{ij,1}\,dA \tag{2}$$

where A is the area enclosed by the contour Γ and ε^{0}_{ij} is an initial strain. ε^{0}_{ij} is related to the residual stress and strain in the residually-stressed object before occurrence of the crack by [15,16]:

$$\varepsilon^{0}_{ij} = -\varepsilon^{el}_{ij}\Big|_{init} = \sigma_{kl}\Big|_{init} S_{ijkl} \tag{3}$$

where ε^{el}_{ij} is elastic strain, S_{ijkl} is the material's compliance tensor, and the suffix $|_{init}$ indicates quantities for the material in a residually-stressed but uncracked "initial" state. Although it does not rigorously characterise the crack tip stress field, Lei's modified J-integral again yields an approximation of the strain energy release rate that can be used as a fracture criterion [3,12,17].

For a cracked structure subjected to load, J and J_{mod} can be calculated explicitly from the results of nonlinear finite element analysis. However, the availability of full-field displacement measurement using Digital Image Correlation (DIC) has led several groups of researchers to

* Corresponding author.
E-mail address: harry.coules@bristol.ac.uk (H.E. Coules).

https://doi.org/10.1016/j.ijmecsci.2018.10.002
Received 27 June 2018; Received in revised form 25 September 2018; Accepted 1 October 2018
Available online 10 October 2018

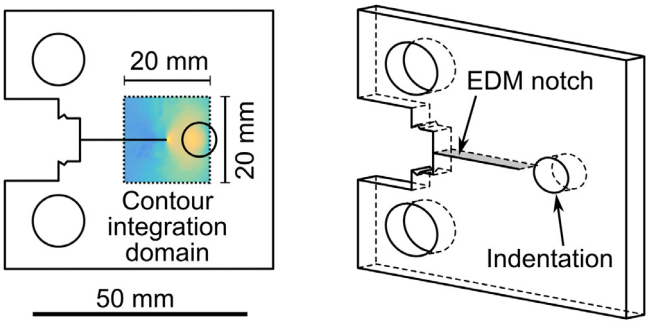

Fig. 1. Geometry of the Compact (Tension) specimens used in fracture initiation tests.

investigate the calculation of J from DIC data. This is useful for validating FE analyses or for determining the J-integral in situations where FEA is not possible. Since DIC only measures an object's surface displacement, the stress and work density terms in Eq. (1) must be inferred from the displacement field using knowledge or assumptions of the material's mechanical constitutive behaviour. Some researchers have used simplified material constitutive relations to allow calculation of σ_{ij} and W, assuming either linear elasticity [18,19] or Ramberg–Osgood deformation plasticity [20]. Others have used a finite element model of the crack tip region, with the displacement field from the DIC result imposed, to implement incremental models of plasticity [21–24]. Both approaches require that:

1. The mechanical constitutive properties of the material are well-characterised.
2. The material is initially in a homogeneous state, or that any initial inhomogeneity (such as non-uniform plastic deformation) can be characterised and accounted for.
3. The material is initially stress-free, or that any initial stress can be characterised and accounted for.

Consequently, for residually-stressed cracks in materials which are inhomogeneous or imperfectly-characterised another approach is needed to enable the determination of J and J_{mod}.

In this study, we have used Energy-Dispersive Synchrotron X-Ray Diffraction (EDXRD) to determine the stress tensor directly during loading of fracture specimens. Using results from both DIC and EDXD, we show that the J-integral can be calculated without reference to the material's inelastic load-elongation response. Additionally, we demonstrate that a material's resistance to ductile tearing initiation can be increased by a non-uniform pattern of prior strain-hardening.

2. Method

2.1. Overview

Tearing initiation tests were performed on thin Compact Tension (C(T)) specimens of ductile steel (see Fig. 1). Two sets of specimens were prepared: prior to cutting of the EDM notch, one set was indented using opposing cylindrical punches applied to either side of the specimen with a force of 75 kN at the location shown in Fig. 1, while the other set was not indented.

The ductile tearing tests were performed on the I12 beamline at the Diamond synchrotron X-ray source. Energy-Dispersive X-Ray Diffraction (EDXRD) was used to determine the stress field in a region surrounding the notch tip at several increments of loading. At the same time, Digital Image Correlation (DIC) was used to determine the distribution of total strain at the specimen's surface. The specimens were loaded until tearing initiation was observed at the notch tip using X-ray radiography (Fig. 2). Further fracture tests were performed under identical conditions but without EDXRD and DIC measurement – these were used to provide additional confirmation of trends in the specimens' load-extension behaviour. EDXRD and DIC data from the fracture tests were used to calculate J_{mod} via the method described in Appendix A and the results were compared with J-integrals calculated from finite element analysis.

2.2. Mechanical constitutive behaviour

All specimens in this study were made from BS 1501-224 28B pressure vessel steel [25]. The material had a roughly equiaxed ferritic–pearlitic microstructure and the average ferrite grain diameter was 17.9 μm (linear intercept method [26]). This is in agreement with previous characterisation of the same material by Balart and Knott [27]. Preliminary uniaxial tensile tests at ambient temperature according to BS 6892-1:2009 [28] were performed on specimens of the steel to determine its mechanical properties. The test specimens had a rectangular cross-section of 12.5×5.0 mm and a parallel length of 80 mm. Tests were performed at a range of loading rates using an Instron 1340 series 100 kN loading frame and an Epsilon Technology Model 3542 axial extensometer with a gauge length of 50 mm.

The results of the tensile tests are shown in Fig. 3. The material was determined to have a Young's modulus of 191 GPa and its plastic deformation was found to be weakly rate-dependent. The loading rate in all subsequent fracture tests was very low, and so all finite element models used constitutive properties based on the results for the lowest available uniaxial loading rate (2.08×10^{-3} s^{-1}). The tensile test data showed very good agreement with previous results for the same material reported by Balart and Knott [27] and Van Gelderen [29].

2.3. Specimen preparation

The Compact (Tension) specimens used in this experiment were extracted from the parent material in the L-T orientation [30]. They were prepared in accordance with the geometry described in ASTM E1820-13 Annex A2.1 [31], except that they had an initial thickness of only 5 mm and were not fatigue pre-cracked. The overall dimensions were $62.5 \times 60 \times 5$ mm. During manufacturing, all cutting was performed using wire Electrical Discharge Machining (EDM). EDM cutting resulted in notch tips that were approximately semi-circular with a radius of 101 ± 3 μm (see Fig. 2); this was verified using calibrated optical microscopy. The use of specimens that were not fatigue pre-cracked was necessary to ensure that each one had the same initial notch length (25.0 ± 0.1 mm) and that the distance from the notch tip to the near side of the indentation was a consistent distance (3.5 ± 0.2 mm). These dimensions were verified using micrometre measurements.

Some C(T) specimens were compressed using a pair of opposed cylindrical indentation tools of BS970-1:1983 817 M40 (EN24) steel with a hardness of 470 HV. The centre of the flat contacting face of each indentation tool was located 7.5 mm ahead of the (future) tip of the EDM notch. Indentation was performed by applying a linearly-ramped compressive load to the tool: 0 kN→75 kN→0 kN at a rate of 625 N s^{-1}. After this process, the mean thickness reduction measured at the centre of the indented region was 0.68 mm; this is identical to the thickness reduction predicted by the FE model. FEA was also used to predict the distribution of plastic strain caused by indentation; this is shown in Fig. 4. A small amount of plastic deformation is predicted to occur where the tip of the notch is later introduced.

2.4. Stress field measurement using EDXRD

During the tearing tests, the stress field in each specimen was determined using Energy-Dispersive X-ray Diffraction (EDXRD) on the I12 beamline at Diamond Light Source. This measurement used a collimated polychromatic beam of synchrotron x-rays from the I12 wiggler source with fixed beam filtration. The energy spectrum of the incident x-rays is described by Drakopoulous et al. [32]. The beam was reduced to a

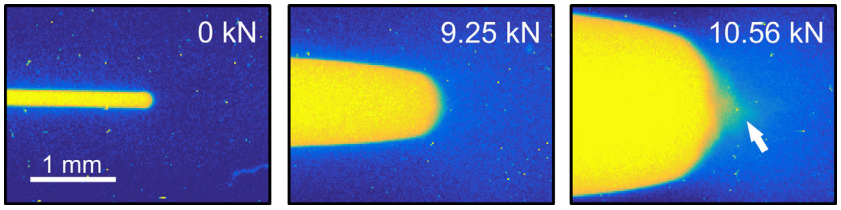

Fig. 2. X-ray radiographs of the notch tip in a non-indented C(T) specimen. Arrow indicates initiation of ductile tearing.

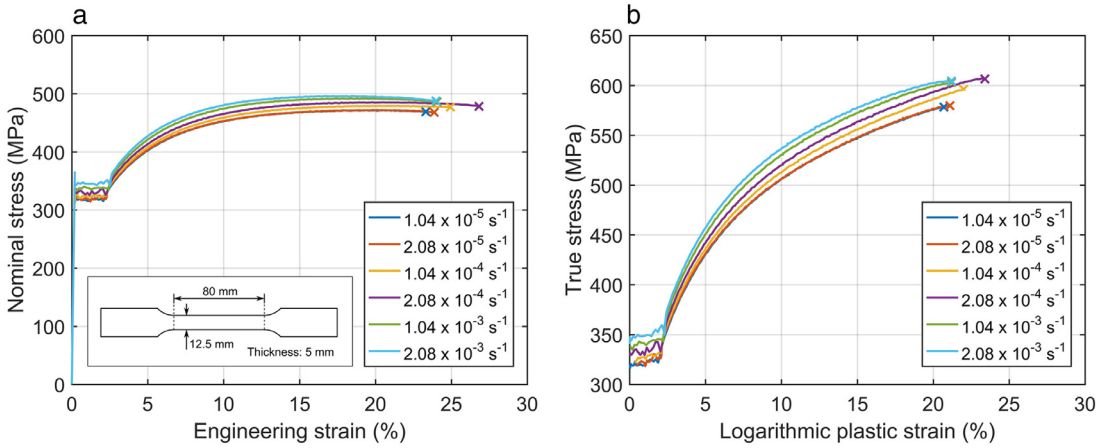

Fig. 3. Ambient-temperature uniaxial tensile test results for BS 1501-224 28B steel at a range of strain rates. (a) Nominal stress vs. strain, (b) True stress vs. plastic strain. Material deformation in the plastic regime is weakly rate-dependent on strain rate range.

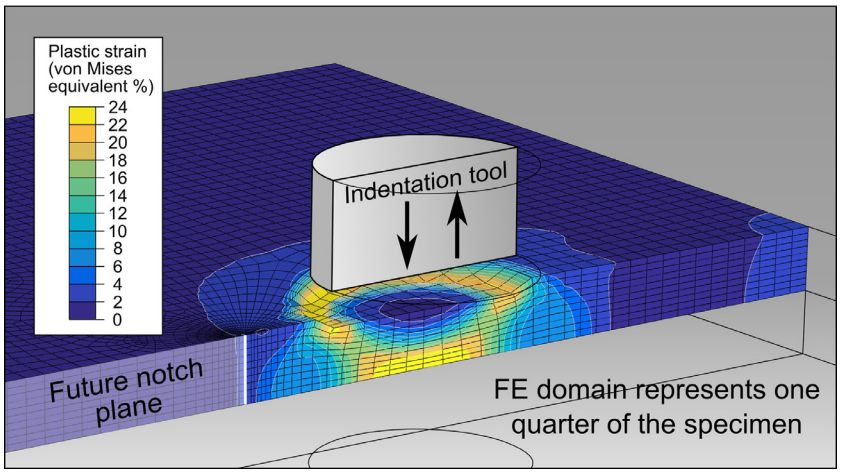

Fig. 4. Predicted distribution of plastic strain around the indented region prior to notch cutting. Only one quarter of the specimen shown due to symmetry.

$100 \times 100\,\mu m$ square cross-section using a pair of slits. The specimen was oriented so that the incident beam was normal to the specimen's surface (see Fig. 5) and positioned so that the centre of the diffraction gauge volume coincided with the specimen's mid-thickness plane. The diffracted beam passed through two semi-circular collimating slits at a scattering angle of $2\theta \cong 4.5°$, and then into a custom-built 23-element detector (Canberra Semiconductor, Olen, Belgium). The detector consisted of a semi-circular array of 23 germanium detector crystals positioned at azimuthal intervals of 8.18° around the axis of the incident beam. Therefore each detector element interrogated a different scattering vector, allowing us to simultaneously measure the material's lattice spacings in 23 directions roughly in the plane of the specimen. The gauge volume was approximately 4.5 mm long (parallel to incident beam) and $100 \times 100\,\mu m$ wide (transverse to the incident beam). During measurement, the specimen and loading rig were translated to scan a rectangular

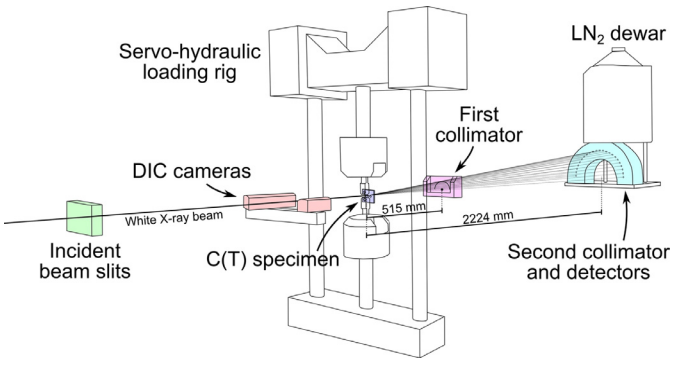

Fig. 5. Experimental setup for EDXRD and DIC measurement of a loaded compact tension specimen on the I12 beamline at Diamond Light Source.

Table 1
Diffraction elastic constants for BS 1501 224 28B steel at ambient temperature.

Diffraction plane	S_1^{hkl} ($m^2 N^{-1} \times 10^{-12}$)	$\frac{1}{2}S_2^{hkl}$ ($m^2 N^{-1} \times 10^{-12}$)
{110}	−1.032(48)	5.850(79)
{200}	−1.971(53)	8.231(88)
{211}	−1.187(42)	5.866(71)
{220}	−1.271(51)	6.092(86)
{310}	−1.857(61)	7.943(102)

array with a spatial resolution of 250 μm within 3 mm of the notch tip and 1000 μm further away, as shown in Fig. 8a. Throughout the experiment, the specimen was kept with its plane normal to the incident beam and not rotated.

Peaks in the energy spectra observed at each detector element were fitted using a Gaussian function. The lattice spacings were calculated from the peak positions using Bragg's law [33]:

$$d^{hkl} = \frac{hc}{2E \sin\theta} \tag{4}$$

where d^{hkl} is the inter-planar spacing of the {hkl} lattice plane family, h is Planck's constant, c is the speed of light and E is the photon energy. For a detector element with azimuthal angle φ, the strain for a given lattice plane family is:

$$\epsilon_\phi^{hkl} = \frac{d_\phi^{hkl} - d_0^{hkl}}{d_0^{hkl}} = p_{ij}^{hkl}\sigma_{ij} \qquad (\text{for } i = 1,2 \text{ and } j = 1,2) \tag{5}$$

where d_ϕ^{hkl} is the observed inter-planar spacing, d_0^{hkl} is the inter-planar spacing measured from a stress-free reference specimen, σ_{ij} is the stress tensor and p_{ij}^{hkl} is a hkl-dependent stress factor tensor. A comb-type reference specimen cut from unstrained material using EDM was used to determine d_0^{hkl}. The stress factors p_{ij}^{hkl} are related to the material's hkl-dependent Diffraction Elastic Constants (DECs) S_1^{hkl} and $\frac{1}{2}S_2^{hkl}$ by:

$$p_{ij}^{hkl} = \begin{cases} \frac{1}{2}S_2^{hkl}h_i^2 + S_1^{hkl} & \text{if } i = j \\ \frac{1}{2}S_2^{hkl}h_i h_j & \text{if } i \neq j \end{cases} \tag{6}$$

where:

$$h = \begin{bmatrix} \cos\phi \\ \sin\phi \end{bmatrix}$$

Inter-planar spacings measured for the {110}, {200}, {211}, {220} and {310} lattice reflections were used in Eq. (5) to form a system of simultaneous linear equations. Only in-plane components of the stress tensor (σ_{11}, σ_{12}, σ_{22}) were included: stresses out of the plane of the specimen (σ_{13}, σ_{23}, σ_{33}) were assumed to sum to zero over the gauge volume. This was then solved in a least-squares sense to determine the stress state at each measured location and the standard uncertainty in stress was determined from the goodness-of-fit. Further details of this analysis method for energy-dispersive data from the I12 beamline are given by Mostafavi et al. [34]. DECs were determined using in-situ uniaxial tensile tests of the material and are given in Table 1. The standard error in the measured stresses was evaluated by propagating the uncertainty in determination of diffraction peak centres through the stress calculation. In this way, the mean standard error for individual measurement points was found to be ±25.8 MPa, although this figure does not include any errors due to material texture effects or uncertainty in gauge volume positioning.

2.5. Strain field measurement using DIC

A Q-400 digital image correlation system (Dantec Dynamics GmbH, Skovlunde, Denmark) was used to measure the 2-dimensional strain field on the specimens' surface. The system comprised a stereo pair of 8-bit greyscale cameras each with 5 megapixel resolution which were positioned to view the specimen's surface at a stand-off distance of approximately 250 mm, which was roughly equal to the cameras' separation distance. 50 mm f2.8 Scheider Kreuznach Xenoplan-0902 lenses were used. In this arrangement, the cameras viewed the measured surface with a resolution of 23 μm/px. Prior to the experiment, the specimens were spray-coated with a black-on-white speckle pattern with an average speckle size of 155 μm. DIC images were recorded at a variable rate as the specimens were loaded, triggering on any specimen displacement of 0.1 mm or load increment of 0.1 kN.

The image data were processed using Istra 4D v4.4.2 (Dantec Dynamics GmbH, Skovlunde, Denmark) to determine the strain field. The correlation algorithm was run using a facet size of 25 pixels and a grid spacing of 5 pixels. The notch tip position was identified manually from the DIC images, allowing its motion during loading to be tracked. The median pointwise uncertainty in the result was evaluated to be ±0.022% strain.

2.6. Predictive finite element analysis

In addition the experimental investigation, deformation of the specimens during indentation and loading was simulated using the finite element method. Only the deformation preceding fracture initiation was modelled – no crack extension criterion was implemented. For the indented specimen, the complete process of indentation, notch cutting and loading was simulated. This was done in two stages: first a model of the indentation process was performed, and the resulting field quantities were used as initial conditions for a separate model of notch cutting and fracture loading [17]. The models assumed a constant temperature of 20 °C and quasi-static loading conditions.

The inelastic mechanical behaviour of the specimen steel was modelled using incremental plasticity theory with a rate-independent von Mises yield locus. The material was assumed to exhibit nonlinear isotropic strain-hardening. In the elastic regime, it was assumed to behave linearly and isotropically with elastic constants $E = 191$ GPa and $\nu = 0.30$. Strain-hardening parameters were determined from the uniaxial tensile test results shown in Fig. 3. The indentation tool was modelled as a rigid body.

The Abaqus/Standard v6.12 finite element solver (Dassault Systèmes, Providence, RI, USA) was used for all models; pre- and post-processing was performed using Abaqus/CAE v6.12. A mesh consisting of 43,060 reduced-integration linear brick elements (see Fig. 6) was used to represent one quarter of the specimen; symmetry about the crack plane and the specimen mid-thickness was assumed. A focussed radial mesh form was used for a region surrounding the crack tip. Preliminary studies confirmed that the result was not sensitive to further mesh refinement. The model results (stress field data, strain field data and load vs. CMOD curves) also agreed well with subsequent experimental observations [35].

3. Results

The indented C(T) specimens sustained an average of 4.2% greater load prior to the onset of unstable tearing than non-indented specimens, at the cost of a 3.2% reduction in dissipated strain energy (Fig. 7). Viscoplastic behaviour was observed in some of the C(T) specimens subjected to EDXRD measurement: as they were held at a constant force to enable EDXRD scanning there were slow increases in loading pin displacement, at a decreasing rate. The horizontal regions some of the load-displacement curves shown in Fig. 7 result from this effect. The viscoplastic response of the material was confirmed using uniaxial tensile tests performed at a range of different loading rates (see Fig. 3).

Stress and strain fields surrounding the notch tip are shown in Fig. 8. The residual stress field resulting from indentation can be seen in Fig. 8a at 0 kN: indented area is clearly visible and the residual stress field is

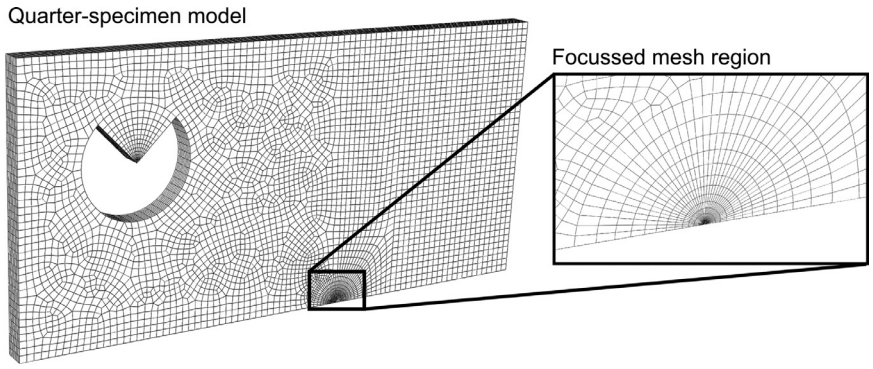

Fig. 6. Finite element mesh used for modelling the C(T) specimens.

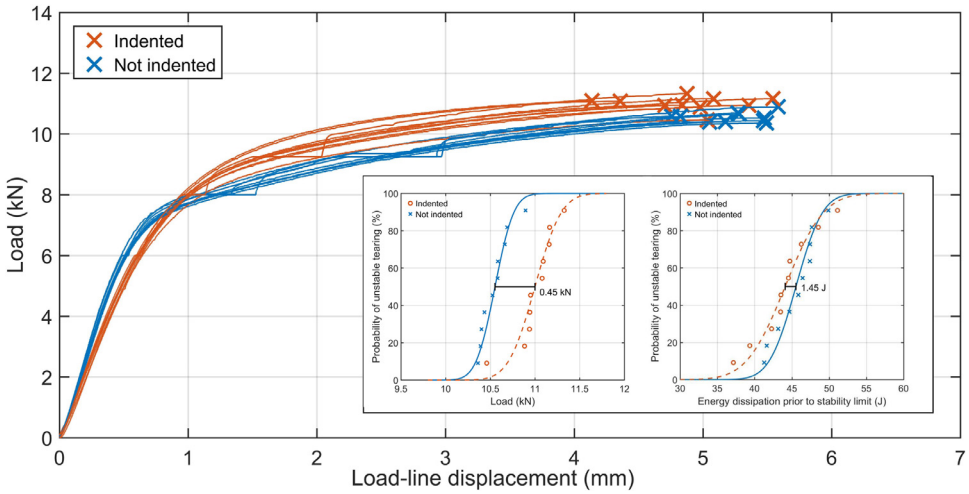

Fig. 7. Load-displacement response of indented and non-indented C(T) specimens ($n = 10$); crosses indicate onset of unstable tearing. Inset figures show Gaussian cumulative distribution functions for load and absorbed strain energy. Indentation produces an increase in mean load capacity of 0.45 kN (4.2%) and a reduction in mean absorbed energy of 1.45 J (3.2%).

also clearly concentrated by the notch tip. The effects of indentation can also be seen in the patterns of stress and strain that subsequently develop during loading (Fig. 8). As the applied load increases to the point where widespread plasticity occurs (8–9.25 kN), prior hardening of the indented specimen allows it to sustain greater stresses ahead of the notch tip. This greatly reduces the amount of localised plastic strain which occurs at the notch tip itself (Fig. 8b) as well as reducing the crack driving force at high levels of applied load.

Fig. 9 shows the elastic–plastic equivalent stress intensity factor K_J as a function of load in the two specimens. K_J was determined independently from experimental DIC and EDXRD results, and from finite element analysis. In each case using Lei's formulation for the J-integral (Eq. (2)) was used. For the non-indented specimen K_J was also calculated through analysis of the load-CMOD curve according to ASME E1820-13 [31]. In cases of plane stress, K_J is related to the J-integral by:

$$K_J = \sqrt{J_{mod} E} \tag{7}$$

Where E is the Young's modulus of the material. In the indented specimen $K_J \approx 50\ \text{MPa}\sqrt{m}$ occurs at zero applied load due to the action of residual stress. In both specimens K_J increases as greater tensile loads are applied, but it increases more rapidly in the non-indented specimen which surpasses the indented specimen at 8.1 kN.

The different methods of determining J_{mod} (and hence K_J) show excellent agreement, although a discrepancy develops between the results from DIC/EDXRD and FEA for the indented specimen at higher levels of applied load (>7 kN). Widespread plasticity develops in the indented specimen at higher loads, including in regions that were previously deformed during indentation. This suggests that the discrepancy in K_J results from the hardening law used for the finite element analysis, which may not accurately follow the real constitutive properties of the material under strongly non-proportional loading conditions.

4. Discussion and conclusions

The ferritic steel studied here is ductile and exhibits moderate strain-hardening (see Fig. 3). In this material, plastic indentation ahead of a notch tip has two consequences: it creates a residual stress field (Fig. 8a, 0 kN) and it causes strain-hardening within a plastic zone around the indented area (Fig. 10). The residual stress loads the notch, causing a finite value of J_{mod} in the absence of applied load. As external loading is applied, plasticity allows the residual stress to relax and the contribution of residual stress to the J-integral decreases (see Fig. 11). By contrast, the strain-hardening effect caused by indentation does not initially contribute to the J-integral but it does change the pattern of plasticity that occurs as the specimen is loaded. During indentation, the greatest strain-hardening occurs directly beneath the indenter, i.e., 7.5 mm ahead of the notch tip in the case of our specimens (see Fig. 10). At high levels of applied load, when plasticity ahead of the notch tip is widespread, greater stresses are sustained by the strain-hardened region than by the same region of a non-indented specimen. This shields the notch tip at high levels of load, reducing the amount of deformation which occurs here (see Fig. 8).

The net effect of these competing phenomena is to increase the crack driving force relative to a non-indented specimen at applied loads less than 8.1 kN, but to reduce it at higher loads (Fig. 11). When ductile tearing initiates (at roughly 11.2 kN) there is no significant residual stress

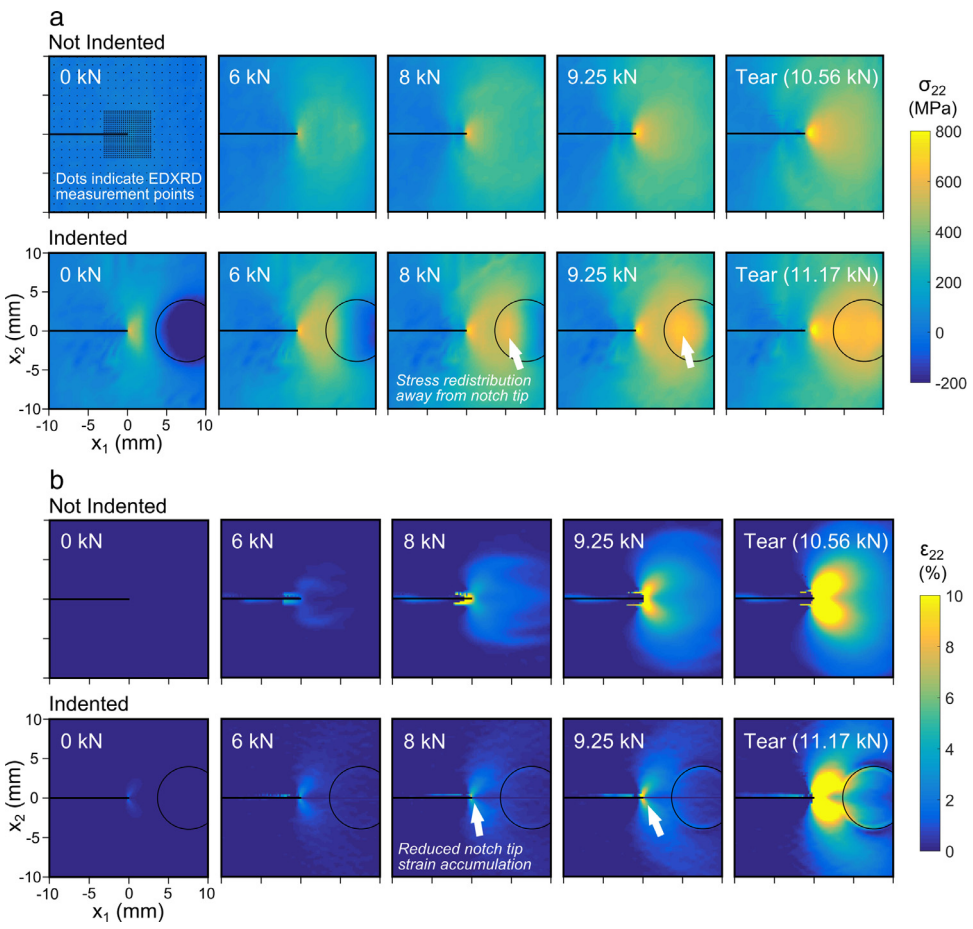

Fig. 8. Measured distributions of stress and strain close to the notch tip during loading of indented and non-indented C(T) specimens. (a) Stress from EDXRD measurements (standard error: ±25.8 MPa), (b) strain from DIC measurements (standard error: ±0.022%).

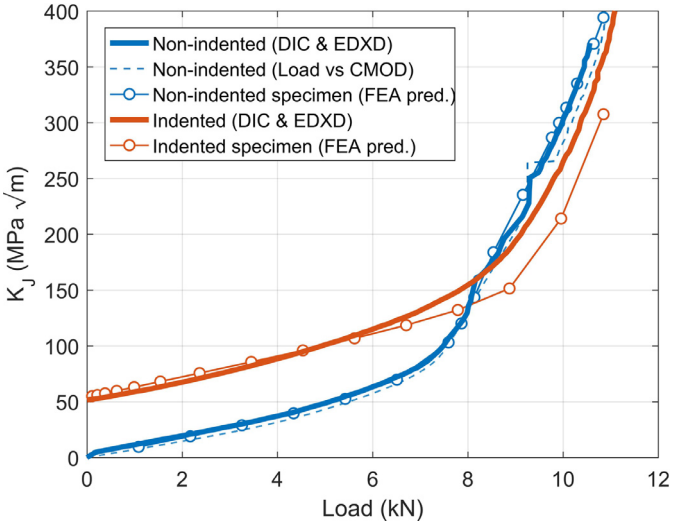

Fig. 9. Elastic–plastic equivalent stress intensity factor K_J as a function of applied load for indented and non-indented specimens, from three methods of analysis.

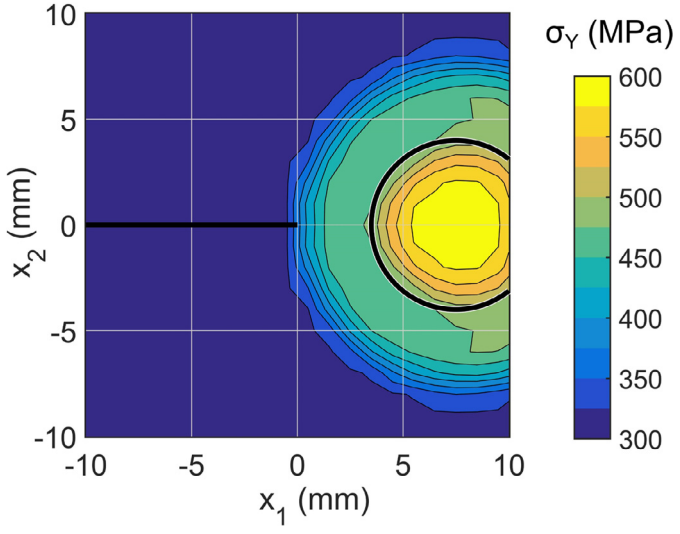

Fig. 10. Yield stress of material at the mid-thickness plane of an indented specimen prior to testing (FEA prediction, note that an isotropic hardening law is assumed). This initial nonuniformity influences the subsequent development of the notch tip stress and strain fields shown in Fig. 8.

contribution to the *J*-integral and the effect of prior strain-hardening dominates. The observation that the *J*-integral at high levels of applied load is suppressed in indented specimens (Fig. 9) is consistent with the fact that these specimens can sustain a greater load prior to the onset of unstable tearing (Fig. 7). This suggests that spatial variations in material load-extension behaviour may be used to control ductile fracture: since

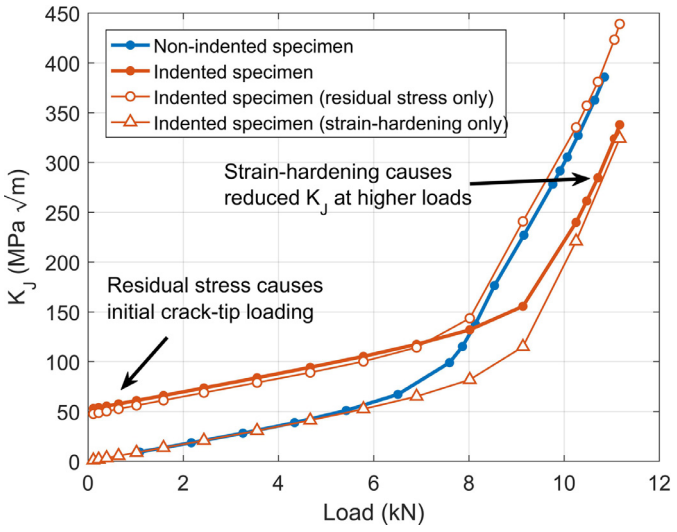

Fig. 11. FEA predictions of the elastic-plastic equivalent stress intensity factor K_J, separating the effects of residual stress and strain-hardening caused by indentation. Residual stress has a dominant effect on K_J when the applied load is low but the consequences of prior strain-hardening dominate at higher loads.

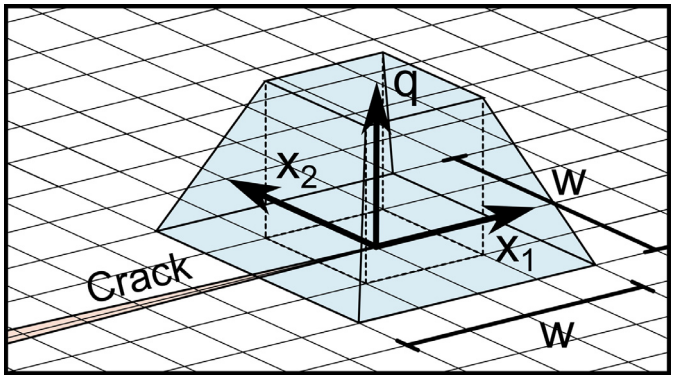

Fig. 12. Plateau function q defined in Eq. (11) and used for evaluating the domain integral of Eq. (10). The width of the plateau is equal to half the overall width of the integration domain. After Shih et al. [37].

prior strain-hardening in the indented specimens can reduce the crack driving force, prior strain-hardening can be used to delay tearing.

Localised prior strain-hardening inhibited tearing initiation in the specimens used for this study. However, several factors limit the range of situations where it could produce a beneficial effect on a material's apparent tearing resistance. Firstly, the material must strain-harden relatively strongly so that the required variation in yield stress can be achieved using localised deformation, without exhausting the material's ductility. Secondly, the mechanism requires that significant plastic deformation must occur in front of the crack tip prior to fracture initiation, and that any detrimental effect of residual stress on initiation is small. Both of these constraints imply that the material must be ductile. Thirdly, the spatial variation that is created in the material's hardening state must act to shield the crack from strain accumulation. Specifically, the material should be strain-hardened in a region which lies at a finite distance ahead of the crack tip, allowing this region to carry a larger force and hence relieving the crack tip zone.

The use of localised strain-hardening to delay ductile tearing can be viewed as an intrinsic toughening mechanism because it inhibits the accumulation of damage in material directly ahead of the notch tip [36]. Most strategies for achieving intrinsic toughening are based on changing a material's micro/nanostructure to promote plastic deformation at the crack tip and/or deflection of the crack path [36]. However in the mechanism reported here, toughening results purely from spatial variations in material load-elongation behaviour. Hardened material ahead of the notch allows greater stresses to be carried there, protecting the notch tip itself. Since the material at the notch tip does not experience large pre-strains, its ductility is maintained. The FEA results in Fig. 11 indicate that this means of toughening does not rely on the presence of a residual stress.

Although the increase in material tearing resistance observed here was relatively small (see Fig. 7), it may be possible to tailor patterns of strain-hardening to produce a larger effect. Exploiting this strengthening mechanism would be advantageous in structures expected to fail via a known mechanism: it would allow designers to optimise a structure's response, trading-off fracture strength in return for increased resistance to plastic collapse. To achieve this, it would be necessary to anticipate the location of tearing initiation so that an appropriate strain-hardening pattern could be introduced.

Previously, several groups of researchers have inferred the J-integral from measurements of the total strain field using finite element analysis [21–24]. This requires that a mechanical constitutive model of the material is assumed so that the stress tensor can be calculated from the measured total strain. In this study, the J-integral was calculated from direct measurements of the stress and total strain fields and we assumed no specific relationship between these fields. This method removes the need for a finite element model of a crack tip boundary layer and can be employed when the mechanical properties of the material are not well characterised – the specimens in this study had an uncharacterised spatially-varying inelastic response. The availability of the stress tensor from EDXRD measurements also allowed us to calculate Lei's modified form of the J-integral directly from measured stress/strain field data for the first time.

Acknowledgements

The authors thank S.J. Oliver and Dr. D.G.A. Van Gelderen for their assistance with the experimental programme. Computer code for J-integral analysis was based on work by Dr T.H. Becker. This project was funded by the UK Engineering and Physical Sciences Research Council under grant no. EP/M019446/1 "Advanced structural analysis for the UK nuclear renaissance". Access to the I12 beamline was provided by Diamond Light Source under proposal no. EE11463.

Data availability statement

Raw and analysed data supporting the findings of this article can be downloaded from: https://doi.org/10.5523/bris.1t6r34y631zff1zdpq0pih5d17.

Appendix A. Calculation of the J-integral from DIC and EDXRD data

The J-integral was calculated from experimentally-measured DIC and EXDRD data using Lei's modified form (J_{mod}) [12]. The specimen was assumed to approximate a state of plane stress throughout the test and a single value of J_{mod} was calculated at each loading state, neglecting any through-thickness variation. For a 20×20 mm square region surrounding the initial notch tip, the stress and total strain tensors σ_{ij} and ε_{ij}, and the displacement vector u_i, were linearly interpolated from their measured locations onto a square grid of 101×101 points. Since the measurement grid used for EDXRD data collection did not change with specimen deformation, the stress measurement locations were compensated using the displacement field measured with DIC:

$$\sigma_{ij}\left(x_i^0\right) = \sigma_{ij}\left(x_i - u_i\right) \tag{8}$$

where x_i is the position vector of an EDXRD measurement location relative to the crack tip, and x_i^0 is its initial position vector. This ensured that each location on the interpolated grid always represented the same

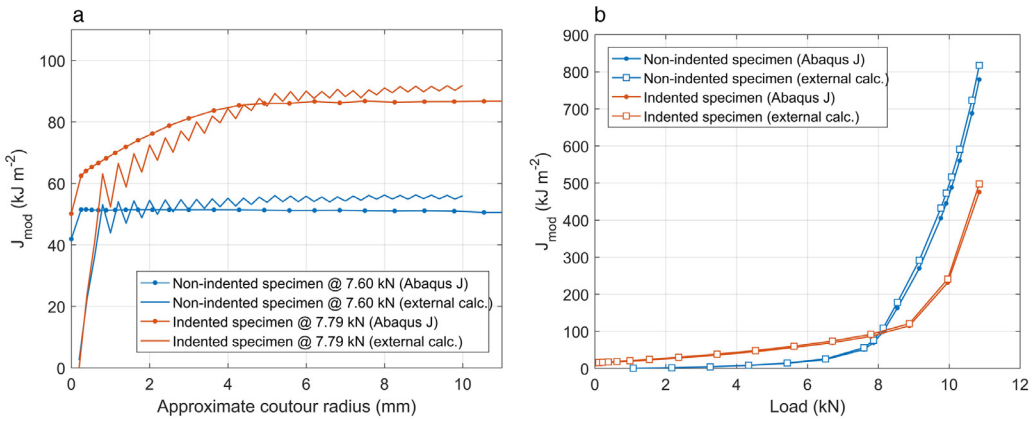

Fig. 13. Comparison of two independent methods of calculating J_{mod} from field data resulting from finite element modelling. (a) Contour convergence of J_{mod} at a single value of applied load. (b) J_{mod} from the last evaluated contour as a function of load.

location in the specimen's initial configuration, despite subsequent deformation during loading.

Although DIC measurements of the total strain field at the specimen's surface were taken continuously during each test, it was only possible to measure the stress field at a small number of loading increments using EDXRD. To estimate the stress field at intermediate increments of loading, the measured stresses were interpolated linearly with respect to the applied load. The strain energy density W at each grid location was calculated by integrating the stress and strain:

$$W = \int_{\varepsilon_{ij}|_{init}}^{\varepsilon_{ij}|_{load}} \sigma_{ij}\varepsilon_{ij}\, d\varepsilon_{ij} \tag{9}$$

Note that any strain energy dissipated as plastic work prior to introduction of the notch is not included in this definition [12]. The modified J-integral was then calculated using the following equivalent domain integral:

$$J_{mod} = \int_A \left(\sigma_{ij}u_{i,1} - W\delta_{1,i}\right)q_{,i} + \sigma_{ij}\varepsilon^0_{ij,1}\, dA \tag{10}$$

The inherent strain ε^0_{ij} was calculated from EDXRD measurements of initial elastic strain using Eq. (3). q is an arbitrary continuous function which takes a value of 0 at the outer edge of the domain and 1 at the crack tip [37]. In this study, a 'plateau' function (Fig. 12) was used:

$$q(x_1,x_2) = \begin{cases} 1 & |x_1| \le \frac{w}{4}, |x_2| \le \frac{w}{4} \\ 2\left(1-\frac{x_2}{w}\right) & \frac{w}{4} < |x_1| \le \frac{w}{2}, \frac{w}{4} < |x_2| \le \frac{w}{2},\ x_2 \ge x_1, x_2 > -x_1 \\ 2\left(1+\frac{x_1}{w}\right) & \frac{w}{4} < |x_1| \le \frac{w}{2}, \frac{w}{4} < |x_2| \le \frac{w}{2}, x_2 > x_1, x_2 \le -x_1 \\ 2\left(1+\frac{x_2}{w}\right) & \frac{w}{4} < |x_1| \le \frac{w}{2}, \frac{w}{4} < |x_2| \le \frac{w}{2}, x_2 \le x_1, x_2 < -x_1 \\ 2\left(1-\frac{x_1}{w}\right) & \frac{w}{4} < |x_1| \le \frac{w}{2}, \frac{w}{4} < |x_2| \le \frac{w}{2}, x_2 < x_1, x_2 \ge -x_1 \\ 0 & \text{otherwise} \end{cases} \tag{11}$$

where w is the side length of the square integration domain A.

To validate the contour integration procedure, it was applied to stress, strain and displacement field data resulting from the finite element models of two specimens and compared with the corresponding values of J_{mod} calculated from the same data by Abaqus/Standard. The FEA results were averaged in the through-thickness direction to give a single value of J_{mod}. Fig. 13a shows that both calculation methods converge quickly to constant values of J_{mod} at large contour radii. Furthermore, there is good agreement between the two calculation methods for all levels of applied force (Fig. 13b). All contour integral results throughout the rest of this article used the from largest evaluated integration domain.

References

[1] Withers PJ. Residual stress and its role in failure. Rep Prog Phys 2007;70(12):2211–64.
[2] Bolinder T, Faleskog J. Evaluation of the influence of residual stresses on ductile fracture. J Press Vessel Technol Trans ASME 2015;137(6):061408.
[3] Coules HE, Horne GCM, Venkata KA, Pirling T. The effects of residual stress on elastic-plastic fracture propagation and stability. Mater Des 2018;143:131–40.
[4] Eshelby JD. The elastic energy-momentum tensor. J Elast 1975;5(3–4):321–35.
[5] Rice JR. A path independent integral and the approximate analysis of strain concentration by notches and cracks. J Appl Mech 1968;35:379–86.
[6] Hutchinson JW. Singular behaviour at the end of a tensile crack in a hardening material. J Mech Phys Solids 1968;16(1):13–31.
[7] Rice JR, Rosengren GF. Plane strain deformation near a crack tip in a power-law hardening material. J Mech Phys Solids 1968;16:1–12.
[8] Begley JA, Landes JD. The J-integral as a fracture criterion. In: Fracture toughness: proceedings of the 1971 national symposium on fracture mechanics, part II (ASTM STP 514). American Society for Testing and Materials; 1972. p. 1–21.
[9] Zhu X-K, Joyce JA. Review of fracture toughness (G, K, J, CTOD, CTOA) testing and standardization. Eng Fract Mech 2012;85:1–46.
[10] Atluri SN, Nishioka T, Nakagaki M. Incremental path-independent integrals in inelastic and dynamic fracture mechanics. Eng Fract Mech 1984;20(2):209–44.
[11] Moran B, Shih CF. Crack tip and associated domain integrals from momentum and energy balance. Eng Fract Mech 1987;27(6):615–42.
[12] Lei Y. J-integral evaluation for cases involving non-proportional stressing. Eng Fract Mech 2005;72(4):577–96.
[13] Lei Y, O'Dowd NP, Webster GA. Fracture mechanics analysis of a crack in a residual stress field. Int J Fract 2000;106(3):195–216.
[14] Wilson WK, Yu I-W. The use of the J-integral in thermal stress crack problems. Int J Fract 1979;15(4):377–87.
[15] Korsunsky AM. Eigenstrain analysis of residual strains and stresses. J Strain Anal Eng Des 2009;44(1):29–43.
[16] Mura T. Micromechanics of defects in solids. Dortrecht, The Netherlands: Kulwer Academic Publishers; 1987.
[17] Lei Y. Validation of contour integral functions (J and C(t)) in ABAQUS v6.11-v6.14 for combined mechanical and residual stresses. Struct Integr Procedia 2016;2:2566–74.
[18] Allaer K, Baere ID, Paepegem WV, Degrieck J. Direct fracture toughness determination of a ductile epoxy polymer from digital image correlation measurements on a single edge notched bending sample. Polym Test 2015;42:199–207.
[19] Wang H-W, Kang Y-L, Zhang Z-F, Qin Q-H. Size effect on the fracture toughness of metallic foil. Int J Fract 2003;123(3–4):177–85.
[20] Yoneyama S, Arikawa S, Kusayanagi S, Hazumi K. Evaluating J-integral from displacement fields measured by digital image correlation. Strain 2014;50(2):147–60.
[21] Barhli SM, Mostafavi M, Cinar AF, Hollis D, Marrow TJ. J-integral calculation by finite element processing of measured full-field surface displacements. Exp Mech 2017;57(6):997–1009.
[22] Becker TH, Mostafavi M, Tait RB, Marrow TJ. An approach to calculate the J-integral by digital image correlation displacement field measurement. Fatigue Fract Eng Mater Struct 2012;35(10):971–84.
[23] Jandejsek I, Gajdoš L, Šperl M, Vavrík D. Analysis of standard fracture toughness test based on digital image correlation data. Eng Fract Mech 2018;182:607–20.
[24] Vavrik D, Jandejsek I. Experimental evaluation of contour J integral and energy dissipated in the fracture process zone. Eng Fract Mech 2014;129:14–25.
[25] BSI. BS 1501-2:1988 Steels for pressure purposes. specification for alloy steels: plates. BSI; 1988.
[26] ASTM. Standard test methods for determining average grain size. ASTM International; 2013. E112–13.

[27] Balart MJ, Knott JF. Effects of geometry and flow properties on the fracture toughness of a C-Mn reactor pressure vessel steel in the lower shelf region. Int J Press Vessels Pip 2006;83(3):205–15.
[28] BSi. 6892-1:2009 Metallic materials – tensile testing – part 1: method of test at ambient temperature. BSi; 2009.
[29] Gelderen DGAV. Effects of load history on low temperature fracture of steels. University of Bristol; 2016.
[30] ASTM. Standard terminology relating to fatigue and fracture testing. ASTM; 2010. E1823–10a.
[31] ASTM. Standard test method for measurement of fracture toughness. ASTM; 2013. E1820–13.
[32] Drakopoulos M, Connolley T, Reinhard C, Atwood R, Magdysyuk O, Vo N, Hart M, Connor L, Humphreys R, Howell G, Davies S, Hill T, Wilkin G, Pedersen U, Foster A, Maio ND, Basham M, Yuan F, Wanelik K. I12: the Joint Engineering, Environment and Processing (JEEP) beamline at Diamond Light Source. J Synchrotron Radiat 2015;22:828–38.
[33] Engler O, Randle V. Introduction to texture analysis: macrotexture, microtexture, and orientation mapping. 2nd ed. CRC Press; 2009.
[34] Mostafavi M, Collins DM, Peel MJ, Reinhard C, Barhli SM, Mills R, Marshall MB, Dwyer-Joyce RS, Connolley T. Dynamic contact strain measurement by time-resolved stroboscopic energy dispersive synchrotron X-ray diffraction. Strain 2017;53:e12221.
[35] Coules HE, Horne GCM, Peel MJ, Oliver SJ, Gelderen DGAV, Connolley T. Direct observation of elastic and plastic strain fields during ductile tearing of a ferritic steel. In: Proceedings of the ASME 2016 pressure vessels & piping conference; 2016 63345.
[36] Ritchie RO. The conflicts between strength and toughness. Nat Mater 2011;10(11):817–22.
[37] Shih CF, Moran B, Nakamura T. Energy release rate along a three-dimensional crack front in a thermally stressed body. Int J Fract 1986;30(2):79–102.